ACS APPLIED MATERIALS & INTERFACES

Research Article

www.acsami.org

Tunnel Conduction in Epitaxial Bilayers of Ferromagnetic $LaCoO_3$/$La_{2/3}Sr_{1/3}MnO_3$ Deposited by a Chemical Solution Method

Irene Lucas,*[†,‡,⊥] José Manuel Vila-Fungueiriño,[§] Pilar Jiménez-Cavero,[‡,⊥] Beatriz Rivas-Murias,[§] César Magén,[†,‡,⊥] Luis Morellón,[‡,⊥] and Francisco Rivadulla[§]

[†]Fundación ARAID, 50018 Zaragoza, Spain

[‡]Departmento Física de la Materia Condensada, Universidad de Zaragoza, Pedro Cerbuna 12, 50009 Zaragoza, Spain

[§]Centro de Investigación en Química Biológica y Materiales Moleculares (CIQUS), Universidad de Santiago de Compostela, 15782 Santiago de Compostela, Spain

[⊥]Instituto de Nanociencia de Aragón (INA), Universidad de Zaragoza, Mariano Esquillor, Edificio I+D, 50018 Zaragoza, Spain

ABSTRACT: We report magnetic and electronic transport measurements across epitaxial bilayers of ferromagnetic insulator $LaCoO_3$ and half-metallic ferromagnet $La_{2/3}Sr_{1/3}MnO_3$ (LCO/LSMO: 3.5 nm/20 nm) fabricated by a chemical solution method. The $I-V$ curves at room temperature and 4K measured with conducting atomic force microscopy (CAFM) on well-defined patterned areas exhibit the typical features of a tunneling process. The curves have been fitted to the Simmons model to determine the height (φ) and width (s) of the insulating LCO barrier. The results yield $\varphi = 0.40 \pm 0.05$ eV (0.50 ± 0.01 eV) at room temperature (4K) and $s = 3$ nm, in good agreement with the structural analysis. Our results demonstrate that this chemical method is able to produce epitaxial heterostructures with the quality required for this type of fundamental studies and applications.

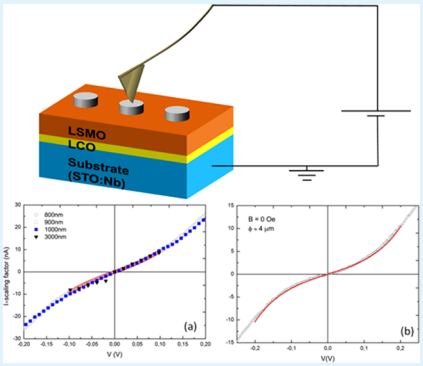

KEYWORDS: *spintronics, tunnel junction, conductive AFM, polymer assisted desposition, thin films, strain-induced ferromagnetism*

INTRODUCTION

The large Hund exchange energy in $La_{2/3}Sr_{1/3}MnO_3$ (LSMO) produces a complete splitting of the majority and minority spin bands,[1] therefore making this material a good source of spin-polarized electrons.[2] Having a T_C well above room temperature (≈360 K), LSMO is therefore an ideal candidate to be used as an electrode in heterostructures for spin tunneling applications.[3−6] On the other hand, the quality of the tunnel barrier in these heterostructures is the main and most critical step to success in the fabrication of high quality magnetic tunnel junctions. Spinel ferrites such as $NiFe_2O_4$ (NFO) and $CoFe_2O_4$ (CFO) have been reported to show spin-filtering effects,[7−11] acting not only as insulating barrier but also selecting the spin orientation due to their ferrimagnetic nature. However, despite their predicted high spin-filtering efficiency at room temperature, all the reports indicate a much lower performance than expected.[12,13] Unfortunately, there are not many intrinsic ferromagnetic oxides that are also good insulators, and therefore alternative strategies for materials design must be developed to advance in this line.

In this regard, bulk magnetic and electric properties of certain perovskite oxides may be engineered on demand by epitaxial growth on a substrate. In particular, it has been shown that $LaCoO_3$ (LCO), which is a diamagnetic insulator in bulk at low temperatures, exhibits a ferromagnetic order under epitaxial tensile-strain below $T < 85$ K,[14−18] combined with a high electrical resistivity.[19] The origin of the ferromagnetism in strained LCO is still under debate:[14,20,21] a complex relaxation mechanism of the epitaxial strain involving ordered stripe patterns of oxygen vacancies was proposed by Biškup et al.[14] In addition, it is well-known that the close proximity between the crystal-field splitting of Co^{3+} in an octahedral oxygen environment and the exchange coupling, produces an activated population of the higher spin states at the expense of the low spin state (LS) in bulk $LaCoO_3$.[22−24] Therefore, other authors[20,21] proposed a novel strain−relaxation mechanism that results in an ordered pattern of locally tetragonal and monoclinic distortions. These produce the coexistence of LS-HS (high spin) Co^{3+}, and introduces the possibility of a ferromagnetic interaction.[17,18] In this direction, Choi et al.[20] reported the existence of a fully strained thin layer of the film of ≈2 nm close to the substrate. Therefore, it is not clear whether thin films of LCO of just a few nanometers compatible with the thicknesses required for the fabrication of tunneling barriers will retain the FM properties. Moreover, different growth methods could differ in the way of relaxing the epitaxial strain. In particular, chemical solution deposition methods imply a growth close to thermodynamic equilibrium, very different from the conditions in pulsed laser deposition (PLD) or sputtering, and therefore the possibility of studying the

Received: September 12, 2014
Accepted: November 13, 2014
Published: November 13, 2014

   dx.doi.org/10.1021/am506259p | ACS Appl. Mater. Interfaces 2014, 6, 21279−21285

magnetism in very thin films and heterostructures prepared by chemical methods becomes interesting. Moreover, chemical methods compared to physical ones such as PLD or sputtering are cheaper because they do not need a vacuum environment.

In this work, we report the fabrication of STO:Nb/LCO/LSMO epitaxial heterostructures by a chemical solution method. Tunneling current between the conducting top electrode LSMO and the conducting substrate of Nb doped $SrTiO_3$ (STO:Nb) was measured across an insulating barrier of LCO ≈ 3.5 nm by conducting tip atomic force microscopy (AFM). A nanostencil lithography technique has been used to define Au nanocontacts of different areas on top of the LSMO surface. The LCO barrier has been structurally characterized showing an epitaxial strained growth along the whole thickness and a sharp interface with the substrate and the LSMO top film. Magnetization measurements confirmed the magnetic nature of the thin barrier. The width (s) and height (φ) of the tunneling barrier between LSMO and LCO have been determined using the Simmons model and are consistent with reported values for insulating barriers used in similar heterostructures.

EXPERIMENTAL SECTION

For the deposition of the LCO/LSMO bilayers, an epitaxial layer of LCO was first crystallized on top of TiO_2-terminated Nb:STO (001).[19,25−27] For this, individual solutions of the cations were prepared by dissolving the corresponding nitrates in water with ethylenediaminetetraacetic acid (EDTA, 1:1 molar ratio) and polyethylenimine (PEI) (1:1 mass ratio to EDTA). Each individual solution was filtrated using Amicon filtration units (10 kDalton), and retained portions were analyzed by inductively coupled plasma (ICP). The solutions were mixed according to the desired final stoichiometry and concentrated to 60 and 120 mM for LCO and LSMO, respectively. Viscosity of solutions was measured in a DMA 4100M (Anton Paar) densimeter, with a microviscometer module (Lovis 2000 ME) resulting in values of 2.5−4 mPa·s. The spin-coating of LCO was performed at 3500 rpm, 20 s (acceleration and deceleration ramp of 250 rpm/s^2) using 30 μL of solution. Under these conditions, a polymeric film typically of 200 nm is obtained. The sample was then ramped (without preannealing) to the final annealing temperature (950 °C) and cooled down at 1 °C/min to avoid cracks. Once this film of LCO is crystallized, the precursor solution of LSMO is spin coated on top of it. 30 μL of this solution was deposited at 4000 rpm, 20 s (acceleration and deceleration ramp of 250 rpm/s^2). The thermal annealing is the same as in the LCO. The films show excellent homogeneity over the whole substrate (5 × 5 mm) with only small imperfections at the corners. Controlling the cationic concentration of the initial solutions we were able to produce bilayers of LCO (3.5 nm) and LSMO (20 nm). The films cover the whole surface of the substrates (5 × 5 mm), with only small imperfections at the corners. Scanning transmission electron microscopy (STEM) characterization of the LCO/LSMO bilayer has been performed in an FEI Titan 60-300 operated at 300 kV and equipped with a high brightness Schottky field emission gun, a CETCOR probe aberration corrector from CEOS to provide a spatial resolution better than 1 Å in STEM mode, and a Gatan Imaging Filter 866 ERS for spectroscopic analysis. Z contrast imaging has been carried out in high angle annular dark field (HAADF) with a probe convergence angle of 25 mrad and an inner collection angle of approximately 58 mrad. HAADF imaging was combined with electron energy loss spectroscopy (EELS) to analyze chemically the heterostructures by spectrum imaging (SI). In this case, both the inner angle for the HAADF detector and the spectrometer collection angle were 60 mrad. SI has been performed with an energy dispersion of 0.5 eV and the dwell time around 0.04 s. The specimen analyzed is a lamella extracted from the sample by focused ion beam (FIB) milling in a FEI Helios Nanolab 600 using a 5 kV ion beam for the final thinning to reduce the surface amorphization layer. LCO thin films have been reported to show pinholes at the surface to release epitaxial strain.[28] Therefore, conventional van der Pauw geometry is not a valid method to measure the electric response. To overcome this problem, nanostencil lithography has been used to deposit Au nanocontacts of different diameters using shadow masks patterned by FIB lithography. CAFM measurements at room temperature were performed using a comercial Veeco-Brucker MultiMode system whereas an Attocube system was used for low temperature measurements. Both systems can be use in conductive mode and the Attocube AFM can be used at temperatures down to 1.5 K and allows us to apply in-plane magnetic fields up to 2 T.

RESULTS AND DISCUSSION

The high-resolution X-ray reciprocal space map of the LCO/LSMO bilayer around the ($\bar{1}03$) is shown in Figure 1a. The

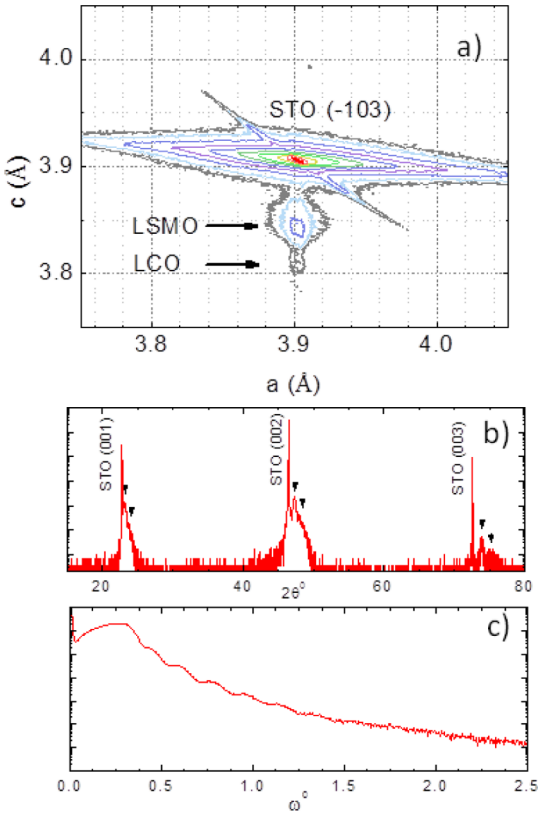

Figure 1. (a) High-resolution X-ray reciprocal space map of the LCO/LSMO bilayer, around the ($\bar{1}03$) peak. (b) X-ray diffraction pattern of the LCO/LSMO bilayer. The arrows indicate the position of the (00l) peaks of LSMO and LCO. (c) X-ray reflectivity curve of the LCO/LSMO bilayer.

peak of the thin LCO layer can be clearly appreciated. There is a perfect in-plane matching of the LCO and LSMO layers to the substrate, confirming the epitaxial growth of the films. This implies a tensile strain of +2.63% for LCO and +0.62% for LSMO, while the out-of-plane lattice parameter reflects a compression of 2.4% for LCO and 1.4% for LSMO. Moreover, only the (00l) peaks are observed between 10° and 120° in the 2Θ-ω scans (Figure 1b), indicating the oriented growth and absence of any spurious phase. Also, the observation of Kiessig fringes in the reflectivity analysis (Figure 1c) confirms the low surface and interface roughness of the layers, and the continuous growth of the films over the substrate. This smoothness over the whole area is exceptional for layers grown by a chemical method, and particularly for a case like this in which a second layer of LSMO is deposited on top of a

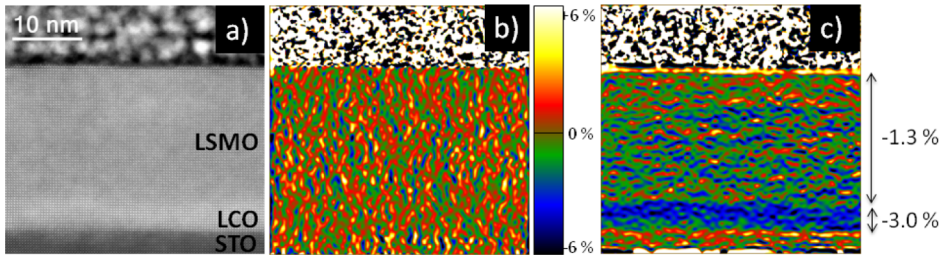

Figure 2. HAADF imaging of the LCO/LSMO bilayer grown on Nb:STO. (a) HAADF image. (b) In-plane and (c) out-of-plane deformation of the lattice parameter with respect to the substrate obtained by GPA. The strong compression of the out-of-plane lattice parameter in LCO is homogeneous through the film.

previously grown film of LCO. The values of the roughness derived from the fitting of the X-ray reflectivity curves and from topography AFM images are respectively 0.7(1) nm and 0.5 (1.3) for all the interfaces and the top surface of LSMO. These values are perfectly comparable to typical values obtained by physical deposition techniques.

The HAADF image of a cross sectional specimen of the bilayer shown in Figure 2a evidences locally the good crystal quality of the bilayer. Both layers grow epitaxial and coherent onto the STO:Nb substrate. They are fully strained with no presence of structural defects, such as misfit dislocations, to accommodate the epitaxial strain. The 3.5 nm thick LCO film can be clearly identified on top of the STO:Nb by the slightly higher intensity with respect to the 20 nm thick LSMO top layer, which is related to the higher average Z number of the La-richer LCO. Over a series of images, we have observed that the thickness of the LCO layer apparently decreases to 2−3 nm. This suggests that the LCO layer presents significant steps at the top surface. Geometrical Phase Analysis (GPA) has been carried out to probe locally the deformation state of the LCO and LSMO layers. The in-plane lattice parameter, Figure 2b, is thoroughly homogeneous, as expected from a fully strained film, whereas the out-of-plane lattice parameter, Figure 2c shows an average out-of-plane lattice parameter for the LCO layer 3.0(5)% smaller than the substrate, whereas the LSMO is 1.3(3)% reduced with respect to the STO:Nb. These values are in very good agreement with the values obtained from X-ray diffraction. It is important to note that these values are consistent with a fully elastic deformation of LSMO, which conserves the volume of the system. However, for LCO, the volume in the tensile strained film increases ≈5% with respect to the bulk. This change must related to a variation in the stoichiometry of the sample, most probably by the generation of oxygen vacancies. The oxygen deficiency of the LCO layer is evidenced in the HAADF image. It presents the typical structure of dark stripes perpendicular to the substrate plane which are a common feature due to the ordering of oxygen vacancies.[29]

The chemical composition of the layers and their interfaces has been explored by STEM-EELS spectrum imaging. The result of a two-dimensional chemical map across the two interfaces is presented in Figure 3. This atomic resolution map shows the atomic structure of the heterostructure with chemical sensitivity. La in A positions forms a square lattice that intermixes with the B-type Co (Mn) columns following the typical perovskite structure. A region where the STO:Nb-LCO interface is extremely sharp is shown, with a thickness in the range of a single lattice cell, and no significant chemical diffusion is observed. The LCO-LSMO interface appears chemically abrupt, with a chemical intermixing due to

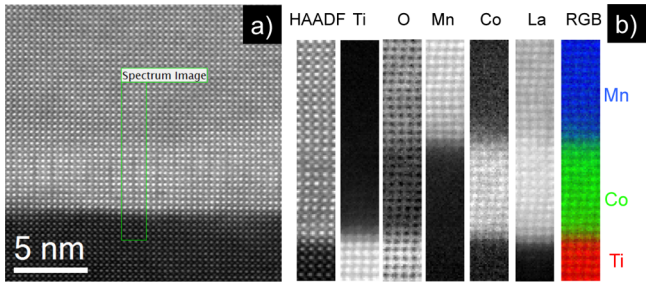

Figure 3. Spectrum imaging of the LCO/LSMO bilayer grown on STO. (a) HAADF reference image. (b) Integrated intensity maps of the simultaneously acquired HAADF, Ti $L_{2,3}$, O K, Mn $L_{2,3}$, Co $L_{2,3}$ and La $M_{4,5}$ signals.

interdiffusion or surface roughness limited to a maximum of about 2 unit cells.

The magnetic properties of the bilayer are summarized in Figure 4. The magnetization of the thin LCO layer is very small, and the diamagnetism of STO dominates the signal at fields larger than ≈100 Oe. For that reason, the M(H) loop for the single layer of LCO is not presented in Figure 4b. In any case, the magnetic transition at $T_C \approx 85$ K is clearly visible, both in the single layer of LCO and in the bilayer, on top of the magnetization of LSMO. These results demonstrate that ≈3.5 nm thick strained films of LCO deposited by this chemical method are still ferromagnetic. On the other hand, the increase in the coercive field of the bilayer with respect to pure LSMO as well as the higher saturation field (Figure 4b), points to an increase in the anisotropy that might be related to an AF coupling of the LCO and LSMO layers at the interface.

The transport properties at room temperature have been determined by CAFM using a silicon tip coated with boron-doped conducting diamond. To obtain well-defined contact areas for CAFM measurements, Au nanocontacts have been defined on the surface of LSMO using square silicon nitride (Si_3N_4) membranes (250 × 250 μm, 200 nm thick) as shadow masks. The membranes have been patterned by FIB defining triangles to deposit nanocontacts ranging between 750 nm and 5 μm, as shown in Figure 5a. Figure 5b shows a topography image (left) and the corresponding current map (right) for nanocontacts of different diameters. Well-defined sharp Au dots were obtained showing higher conductivity than LSMO surface, as expected. The procedure to perform CAFM measurements is well established and is based on the current flow from the AFM ground to the upper layer of the sample and through the tip effective contact area. This effective AFM tip contact area can be difficult to determine due to the shape of the tip and given that it depends on the applied force. This problem is overcome using the nanostructured contact geometry so that injected

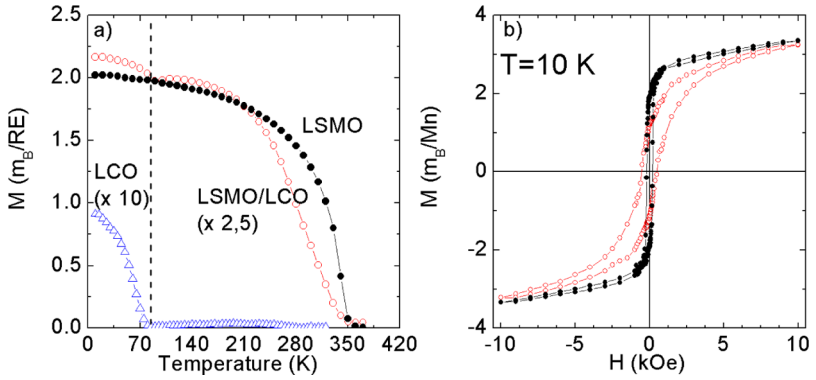

Figure 4. (a) Temperature dependence of the magnetization of a 20 nm thick film of LSMO, a ≃ 3.5 nm thick layer of LCO, and the LCO/LSMO bilayer, at H = 100 Oe. The FM contribution of LCO is visible in the bilayer below the T_C = 85 K. (b) Field dependence of the magnetization at 10 K for a single layer of LSMO (black circles) and for the LCO/LSMO bilayer (red open circles).

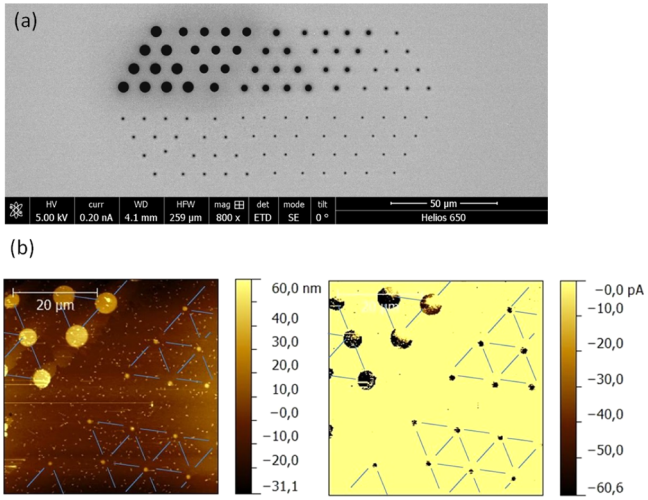

Figure 5. (a) Silicon nitride membrane to be used as shadow mask patterned using FIB lithography. Every triangle allows to deposit a group of 10 Au contacts with same diameter, ranging from 5 μm to 750 nm. (b) Topography image (left) and corresponding current map (right) of Au nanocontacts of different diameters (5 μm, 4 μm, 900 nm, 850 and 800 nm) evaporated on the LSMO surface.

current depends only on the size of the Au dots. Conductive AFM measurements using contact geometry have been achieved so far in Au/LCMO interfaces fabricated by sputtering.[30−32]

AFM topography of the LCO surface prior to the deposition of the LSMO layer showed a large number of pinholes ≈1 μm diameter, with an average distance between them around 5 μm. Thus, the larger contacts can easily cover part of these pinholes and give Ohmic curves by direct contact between LSMO and the substrate. On the other hand, contact diameters below 5 μm give consistent results showing only some small dispersion associated with experimental fluctuations of the tunnel current through an insulating barrier between two conducting layers. These fluctuations follow a log-normal distribution[33] and therefore a logarithmic average was performed for every series of $I-V$ experimental curves measured for every contact size. Figure 6a shows $I-V$ averaged curves characteristic of tunnel current corresponding to the LSMO/LCO bilayer for different Au contact sizes. The intensity measured for every voltage value scales with the contact size, as expected.

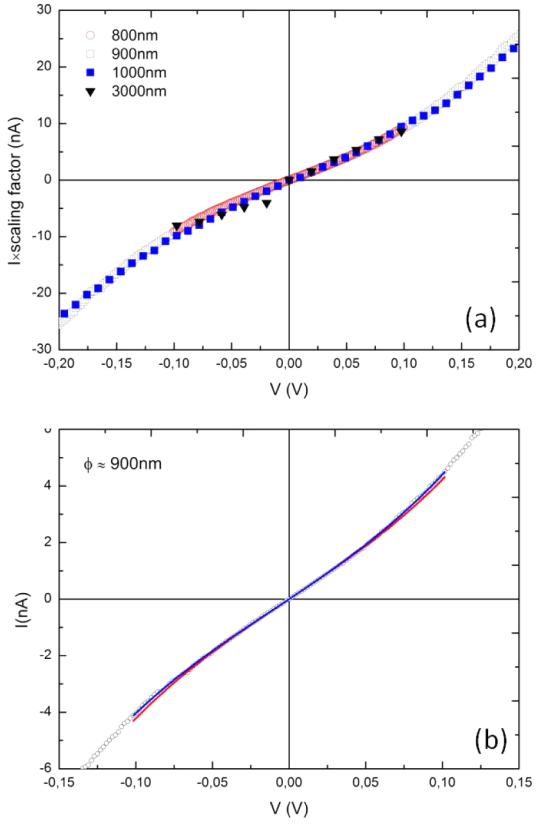

Figure 6. (a) Scaling of the $I-V$ averaged curves as a function of the Au contact diameter measured at room temperature by direct contact of the conducting AFM tip on contacts with diameter ranging from 3 μm to 800 nm. (b) Averaged $I-V$ curve corresponding to a 900 nm Au contact showing the fit to the Simmons model (red line) and to the Brinkman model (blue line).

To prove the quality of the tunneling barrier, the values of resistance per area (RA) at zero bias voltage have been calculated from the reported $I-V$ curves. The values of RA obtained at 300 and 4K are 160 and 5 Ω cm^2, respectively. This proves the negative temperature coefficient of the tunneling resistance, and therefore the good quality of the barrier.[34]

To determine the width and height of the tunnel barrier, the $I-V$ curves have been fitted to the Simmons model[35] in the intermediate voltage range, assumming an isotropic barrier (eq 1). Furthermore, the robustness of the results was tested by the Brickman model (eq 2) to evaluate the case of an anisotropic

barrier.[36] A representative example is shown in Figure 6b. The height and width of the barrier obtained from the fitting are φ = 0.46 ± 0.01 eV and s = 2.7 ± 0.1 nm, respectively, in the case of the Simmons model and φ_{av} = 0.46 ± 0.02 eV and s = 2.7 ± 0.2 nm in the case of the Brinkman model. The same fits were repeated for the different contact sizes using the Simmons model, resulting in an average height φ = 0.40 ± 0.05 eV and width s = 3.2 ± 0.4 nm. This value of s is very close to the thickness of the LCO layer extracted from STEM images (t = 3.5 ± 0.2 nm). Also, the value obtained for φ in the LCO barrier is comparable to previously reported in a LSMO/STO(3−5 nm)/LSMO heterostructures ($\varphi \approx$ 0.5−0.7 eV),[37] and LCMO/STO(3 nm) ($\varphi \approx$ 0.6 eV).[31,32]

$$J = \frac{e}{2\pi h s^2}\left\{\left(\frac{2\varphi - eV}{2}\right)\exp\left[-(2m)^{1/2}\frac{4\pi s}{h}\left(\frac{2\varphi - eV}{2}\right)^{1/2}\right] - \left(\frac{2\varphi + eV}{2}\right)\exp\left[-(2m)^{1/2}\frac{4\pi s}{h}\left(\frac{2\varphi + eV}{2}\right)^{1/2}\right]\right\} \quad (1)$$

$$J = G(0)\left(V - \frac{4\sqrt{2ms}}{3\hbar}\frac{\Delta\varphi}{16\bar{\varphi}^{3/2}}eV^2 + \frac{9}{128\bar{\varphi}}\left(\frac{4\sqrt{2ms}}{3\hbar}\right)^2 e^2 V^3\right) \quad (2)$$

Therefore, these results demonstrate that thin layers of LCO fabricated by this chemical method retain a good insulator character and can be used as tunneling barriers with LSMO at room temperature.

To prove the possibility of the LCO barrier to act as a spin-filter, CAFM measurements were performed below the Curie temperature of LCO under different applied fields. The results obtained at low temperatures are much more reproducible, and the values of the barrier s and φ are practically the same for every contact size. Figure 7a shows tunnel current curves obtained at low temperatures under fields ranging from −500 to +500 Oe. No field dependence was observed; therefore, the system does not act as an efficient spin filter. The values of s and φ from the fit to the Simmons model show no change in the barrier width with respect to room temperature, as expected. However, there is an increase of 0.1 eV in the barrier height. It is worth mentioning that room temperature measurements were repeated using the second AFM system before cooling the sample to confirm the reproducibility of the measurement. The same values of φ and s were obtained in both AFM equipment at room temperature.

Given the possibility of Co to diffuse into the LSMO layer, the formation of a Co/Mn spinel of the type $CoMn_2O_4$ could be a possibility to explain the increase of φ. However, in this case, the size of the barrier should be also modified. Alternatively, a favorable redox reaction between Co^{3+} and Mn^{3+} to produce Co^{2+} and Mn^{4+}, will introduce a Co^{2+}−O−Co^{2+} AF interaction at the interface. Looking at the magnetic data of Figure 4, the decrease of the T_C of LSMO observed in the bilayer with respect to isolated LSMO films, and the decrease of its volume magnetization, makes this possibility very probable.

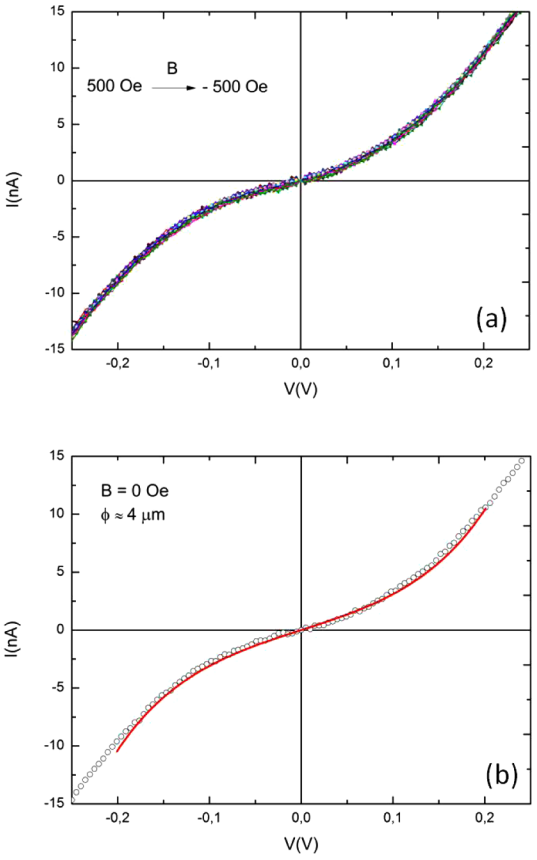

Figure 7. (a) I−V curves measured on a 4 μm contact at 4K applying magnetic field in-plane ranging between −500 and +500 Oe. (b) Averaged I−V curve for a 4 μm contact showing the fit to the Simmons model (red line).

CONCLUSIONS

In summary, we have demonstrated that tunnel heterostructures of LCO/LSMO can be fabricated by a simple chemical solution method. Our results show that ≈3.5 nm thick strained films of LCO still show ferromagnetic behavior. An increase in the coercive field of the bilayer with respect to pure LSMO is observed, as well as a higher saturation field, pointing to an increase in the anisotropy that could be related to an AF coupling of the LCO and LSMO layers at the interface. The I−V curves measured across the tunneling barrier with a CAFM scale with the contact size, and were correctly fitted to the Simmons model. The room temperature value of φ = 0.40 ± 0.05 eV is in good agreement with previous reports for insulating barriers used in similar heterostructures, while the value estimated for s = 3.2 ± 0.4 nm is confirmed by the thickness of the LCO barrier measured by STEM. These results enhance the possibility of using LCO as a suitable insulating barrier in oxide-based magnetic tunnel junctions.

AUTHOR INFORMATION

Corresponding Author

*I. Lucas. E-mail: ilucas@unizar.es.

Notes

The authors declare no competing financial interest.

■ ACKNOWLEDGMENTS

The authors aknowledge the support to this work from Spanish Ministry of Science through project Nos. MAT2011-28532-C03-02, MAT2013-44673-R, and MAT2011-27553-C02 including FEDER funding, the Aragón Regional Government (Project No. E26), ERC-StG-259082(2DTHERMS) and Xunta de Galicia (2012-CP071). Jose Manuel Vila-Fungueiriño aknowledges MINECO of Spain for support through the FPI program, and Irene Lucas and Cesar Magen aknowledge Fundación Aragonesa para la I+D for support through ARAID program.

■ REFERENCES

(1) Park, J. H.; Vescovo, E.; Kim, H. J.; Kwon, C.; Ramesh, R.; Venkatesan, T. Direct Evidence for a Half-Metallic Ferromagnet. *Nature* **1998**, *392*, 794−796.

(2) Owen, M.; Bibes, M.; Barthélémy, A.; Contour, J. P.; Anane, A.; Lemaitre, Y.; Fert, A. Nearly Total Spin Polarization in $La_{2/3}Sr_{1/3}MnO_3$ from Tunneling Experiments. *Appl. Phys. Lett.* **2003**, *82*, 233−235.

(3) Bibes, M.; Barthélémy, A. Oxide Spintronics. *IEEE Trans. Electron Devices* **2007**, *54*, 1003−1023.

(4) Opel, M. Spintronic Oxides grown by Laser-MBE. *J. Phys. D: Appl. Phys.* **2012**, *45*, 033001.

(5) Bibes, M.; Villlegas, J. E.; Barthélémy, A. Ultrathin Oxide Films and Interfaces for Electronics and Spintronics. *Adv. Phys.* **2011**, *60*, 5−84.

(6) Hueso, L. E.; Pruneda, J. M.; Ferrari, V.; Burnell, G.; Valdes-Herrera, J. P.; Simons, B. D.; Littlewood, P. B.; Artacho, E.; Fert, A.; Mathur, N. D. Transformation of Spin Information into Large Electrical Signals using Carbon Nanotubes. *Nature* **2007**, *445*, 410−413.

(7) Luders, U.; Bibes, M.; Bouzehouane, K.; Jacquet, E.; Contour, J. P.; Fusil, S.; Bobo, J. F.; Fontcuberta, J.; Barthelemy, A.; Fert, A. Spin Filtering through Ferrimagnetic $NiFe_2O_4$ Tunnel Barriers. *Appl. Phys. Lett.* **2006**, *88*, 082505.

(8) Luders, U.; Barthelemy, A.; Bibes, M.; Bouzehouane, K.; Fusil, S.; Jacquet, E.; Contour, J. P.; Bobo, J. F.; Fontcuberta, J.; Fert, A. $NiFe_2O_4$: A versatile Spinel Material brings new Opportunities for Spintronics. *Adv. Mater.* **2006**, *18*, 1733−1736.

(9) Chapline, M. G.; Wang, S. X. Room-Temperature Spin Filtering in a $CoFe_2O_4/MgAl_2O_4/Fe_3O_4$ Magnetic Tunnel Barrier. *Phys. Rev. B* **2006**, *74*, 014418.

(10) Ramos, A. V.; Guittet, M.-J.; Moussy, J.-B.; Mattana, R.; Deranlot, C.; Petroff, F.; Gatel, C. Room Temperature Spin Filtering in Epitaxial Cobalt-Ferrite Tunnel Barriers. *Appl. Phys. Lett.* **2007**, *91*, 122107.

(11) Foerster, M.; Rigato, F.; Bouzehouane, K.; Fontcuberta, J. Tunnel Transport through $CoFe_2O_4$ Barriers investigated by Conducting Atomic Force Microscopy. *J. Phys. D: Appl. Phys.* **2010**, *43*, 295001.

(12) Chen, Y. F.; Ziese, M. Spin filtering in $La_{0.7}Sr_{0.3}MnO_3/CoFe_2O_4/Nb(0.5\%)$: $SrTiO_3$ Heterostructures. *Phys. Rev. B* **2007**, *76*, 014426.

(13) Takahashi, Y. K.; Kasai, S.; Furubayashi, T.; Mitani, S.; Inomata, K.; Hono, K. High Spin-Filter Efficiency in a Co Ferrite Fabricated by a Thermal Oxidation. *Appl. Phys. Lett.* **2010**, *96*, 072512.

(14) Biskup, N.; Salafranca, J.; Mehta, V.; Oxley, M. P.; Suzuki, Y.; Pennycook, S. J.; Pantelides, S. T.; Varela, M. Insulating Ferromagnetic $LaCoO_3$-delta Films: A Phase Induced by Ordering of Oxygen Vacancies. *Phys. Rev. Lett.* **2014**, *112*, 087202.

(15) Fuchs, D.; Arac, E.; Pinta, C.; Schuppler, S.; Schneider, R.; von Löhneysen, H. V. Tuning the Magnetic Properties of $LaCoO_3$ Thin Films by Epitaxial Strain. *Phys. Rev. B* **2008**, *77*, 014434.

(16) Park, S.; Ryan, P.; Karapetrova, E.; Kim, J. W.; Ma, J. X.; Shi, J.; Freeland, J. W.; Wu, W. D. Microscopic Evidence of a Strain-Enhanced Ferromagnetic State in $LaCoO_3$ Thin Films. *Appl. Phys. Lett.* **2009**, *95*, 072508.

(17) Sterbinsky, G. E.; Ryan, P. J.; Kim, J.-W.; Karapetrova, E.; Ma, J. X.; Shi, J.; Woicik, J. C. Local Atomic and Electronic Structures of Epitaxial Strained $LaCoO_3$ Thin Films. *Phys. Rev. B* **2012**, *85*, 020403.

(18) Hsu, H.; Blaha, P.; Wentzcovitch, R. M. Ferromagnetic Insulating State in Tensile-Strained $LaCoO_3$ Thin Films from LDA +U Calculations. *Phys. Rev. B* **2012**, *85*, 140404.

(19) Rivadulla, F.; Bi, Z. X.; Bauer, E.; Rivas-Murias, B.; Vila-Fungueiriño, J. M.; Jia, Q. X. Strain-Induced Ferromagnetism and Magnetoresistance in Epitaxial Thin Films of $LaCoO_3$ Prepared by Polymer-Assisted Deposition. *Chem. Mater.* **2013**, *25*, 55−58.

(20) Choi, W. S.; Kwon, J. H.; Jeen, H.; Hamann-Borrero, J. E.; Radi, A.; Macke, S.; Sutarto, R.; He, F. Z.; Sawatzky, G. A.; Hinkov, V.; Kim, M.; Lee, H. N. Strain-Induced Spin States in Atomically Ordered Cobaltites. *Nano Lett.* **2012**, *12*, 4966−4970.

(21) Kwon, J. H.; Choi, W. S.; Kwon, Y. K.; Jung, R.; Zuo, J. M.; Lee, H. N.; Kim, M. Nanoscale Spin-State Ordering in $LaCoO_3$ Epitaxial Thin Films. *Chem. Mater.* **2014**, *26*, 2496−2501.

(22) Haverkort, M. W.; Hu, Z.; Cezar, J. C.; Burnus, T.; Hartmann, H.; Reuther, M.; Zobel, C.; Lorenz, T.; Tanaka, A.; Brookes, N. B.; Hsieh, H. H.; Lin, H.-J.; Chen, C. T.; Tjeng, L. H. Spin State Transition in $LaCoO_3$ Studied using Soft X-ray Absorption Spectroscopy and Magnetic Circular Dichroism. *Phys. Rev. Lett.* **2006**, *97*, 176405.

(23) Yan, J. Q.; Zhou, J. S.; Goodenough, J. B. Bond-Length Fluctuations and the Spin-State Transition in $LCoO_3$ (L=La, Pr, and Nd). *Phys. Rev. B* **2004**, *69*, 134409.

(24) Goodenough, J. B. Metallic Oxides. *Prog. Solid State Chem.* **1971**, *5*, 145−399.

(25) Cobas, R.; Munoz-Perez, S.; Cadogan, J. M.; Puig, T.; Obradors, X. Magnetoresistance in Epitaxial Thin Films of $La_{0.85}Ag_{0.15}MnO_3$ Produced by Polymer Assisted Deposition. *Appl. Phys. Lett.* **2011**, *99*, 083113.

(26) Jia, Q. X.; Mccleskey, T. M.; Burrell, A. K.; Lin, Y.; Collis, G. E.; Wang, H.; Li, A. D. Q.; Foltyn, S. R. Polymer-Assisted Deposition of Metal-Oxide Films. *Nat. Mater.* **2004**, *3*, 529−532.

(27) Vila-Fungueiriño, J. M.; Rivas-Murias, B.; Rodríguez González, B.; Rivadulla, F. Interface Magnetic Coupling in Epitaxial Bilayers of $La_{0.92}MnO_3/LaCoO_3$ Prepared by Polymer-Assisted Deposition. *Chem. Mater.* **2014**, *26*, 1480−1484.

(28) Vila-Fungueiriño, J. M.; Rivas-Murias, B.; Rivadulla, F. Strong Interfacial Magnetic Coupling in Epitaxial Bilayers of $LaCoO_3/LaMnO_3$ Prepared by Chemical Solution Deposition. *Thin Solid Films* **2014**, *553*, 81−84.

(29) Klenov, D. O.; Donner, W.; Foran, B.; Stemmer, S. Impact of Stress on Oxygen Vacancy Ordering in Epitaxial $(La_{0.5}Sr_{0.5})CoO_3$-Partial Derivative Thin Films. *Appl. Phys. Lett.* **2003**, *82*, 3427−3429.

(30) Balcells, L. I.; Abad, L. I.; Rojas, H.; Martinez, B. Material Damage Induced by Nanofabrication Processes in Manganite Thin Films. *Nanotechnology* **2008**, *19*, 135307.

(31) Balcells, L. I.; Abad, L. I.; Rojas, H.; Del Pino, A. P.; Estrade, S.; Arbiol, J.; Peiro, F.; Martinez, B. Transport Properties across the $La_{2/3}Ca_{1/3}MnO_3/SrTiO_3$ Heterointerface. *J. Appl. Phys.* **2008**, *103*, 07E303.

(32) Balcells, L. I.; Abad, L. I.; Rojas, H.; Del Pino, A. P.; Estrade, S.; Arbiol, J.; Peiro, F.; Martinez, B. Electronic Effects in Manganite/Insulator Interfaces: Interfacial Enhancement of the Insulating Tunneling Barriers. *Small* **2008**, *4*, 365−371.

(33) Da Costa, V.; Romeo, M.; Bardou, F. Statistical Properties of Currents Flowing through Tunnel Junctions. *J. Magn. Magn. Mater.* **2003**, *258*, 258−259.

(34) Jonnson-Akerman, B. J.; Escudero, R.; Leighton, C.; Kim, S.; Schuller, I. K.; Rabson, D. A. Reliability of Normal-State Current-Voltage Characteristics as an Indicator of Tunnel-Junction Barrier Quality. *Appl. Phys. Lett.* **2000**, *77*, 1870−1872.

(35) Simmons, J. G. Electric Tunnel Effect between Dissimilar Electrodes Separated by a Thin Insulating Film. *J. Appl. Phys.* **1963**, *34*, 2581.
(36) Brinkman, W. F.; Dynes, R. C.; Rowell, J. M. Tunneling Conductance of Asymmetrical Barriers. *J. Appl. Phys.* **1970**, *41*, 1915−1921.
(37) Sun, J. Z.; Krusin-Elbaum, L.; Duncombe, P. R.; Gupta, A.; Laibowitz, R. B. Temperature Dependent, Non-Ohmic Magnetoresistance in Doped Perovskite Manganate Trilayer Junctions. *Appl. Phys. Lett.* **1997**, *70*, 1769−1771.